

Hierarchical microstructure constructed with graphitic carbon-coated Ni₃S₂ nanoparticles anchored on N-doped mesoporous carbon nanoflakes for optimized sodium storage †

 Author and affiliation details can be edited in the panel that appears to the right when you click on the author list.

Jia-Lin Xu^a, Qiang Sun,^{(ID 0000-0003-1197-1358)^{a,*}}, Hao-Jie Chen^a, Wen-Jie Yan^a and Pai Lu^{a,*}

^aSchool of Metallurgy, Northeastern University, Shenyang 110819, P. R. China, sunq@smm.neu.edu.cn,
lup@smm.neu.edu.cn

Funding Information

 We have combined the funding information you gave us on submission with the information in your acknowledgements. This will help ensure the funding information is as complete as possible and matches funders listed in the Crossref Funder Registry.

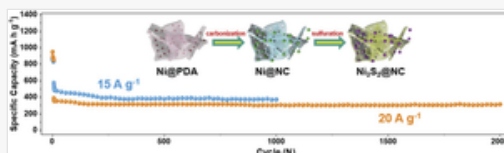
Please check that the funder names and award numbers are correct. For more information on acknowledging funders, visit our website: <http://www.rsc.org/journals-books-databases/journal-authors-reviewers/author-responsibilities/#funding>.

Funder Name :	National Natural Science Foundation of China
Funder's main country of origin :	
Funder ID :	10.13039/501100001809
Award/grant Number :	5190204421503033

Funder Name :	Fundamental Research Funds for the Central Universities
Funder's main country of origin :	
Funder ID :	10.13039/501100012226
Award/grant Number :	N2025021

Table of Contents Entry

Figure Replacement Requested



A hierarchical microstructure constructed with graphitic-carbon-coated Ni₃S₂ nanoparticles anchored on N-doped mesoporous carbon nanoflakes was fabricated using a nickel-based micro-nano structure as a precursor and polydopamine as a carbon source.

Replacement Image: TOC.tif

Replacement Instruction: Replace image requested

Abstract

A hierarchical microstructure constructed with graphitic-carbon-coated Ni₃S₂ nanoparticles anchored on N-doped mesoporous carbon nanoflakes was fabricated using a nickel-based micro–nano structure as a precursor and polydopamine as a carbon source. By optimizing the microstructure, the obtained Ni₃S₂/carbon composite compounded with the thickest carbon nanoflakes delivers ultrafast and stable Na-ion storage performance, and can maintain a reversible charge capacity of 372 mA h g⁻¹ at a current density of 5 A g⁻¹ over 250 cycles, and 316 mA h g⁻¹ even at a current density of 20 A g⁻¹ for 2000 cycles. These remarkable electrochemical properties can be attributed to its hierarchical microstructure of graphitic-carbon-coated Ni₃S₂ particles and N-doped mesoporous carbon nanoflakes, which provide easy accessibility to the electrolyte, fast electron transport and Na⁺ diffusion, and even relieve the strain caused by the volume expansion upon cycling.

Introduction

In recent years, sodium-ion batteries (SIBs) have been considered as the most promising alternative to replace lithium-ion batteries (LIBs) due to the abundant natural reserves of sodium and their almost worldwide distribution.^{1–5} As sodium and lithium have similar physical and chemical properties, drawing on the advanced cathodes of LIBs, significant progress has been made in SIB cathodes with acceptable performance.^{6–8} However, the current commercial graphite for LIB anodes cannot be applied to SIBs because of the mismatch with the larger sodium ion radius and the thermodynamic instability of the sodium–graphite system.^{9–13} Therefore, developing a high-performance anode has become the critical problem for the development of SIBs.¹⁴

Nickel sulfide (Ni₃S₂)^{15–17} is a type of transition-metal sulfide^{18–22} that features an inherent open-frame structure, large interlayer spacing, and lower resistivity. When Ni₃S₂ is used as an SIB anode, it can tolerate the larger sodium ion and store sodium through the conversion mechanism, giving a high theoretical capacity.^{23–25} However, the low conductivity of Ni₃S₂, serious volume changes during the cycle, and the formation of the intermediate polysulfide have led to poor rate performance and rapid capacity degradation at high charge currents.^{26,27} Generally, the synthesis of nanoscale Ni₃S₂ has been an effective strategy to promote the performance of SIBs, as the nanosized structure can increase the number of active sites and the contact area between the anode and the electrolyte, shortening the diffusion paths of electrons and ions. In addition, combining carbon materials, *i.e.*, graphene,²⁸ carbon nanotubes,²⁹ and porous carbon,^{30,31} with Ni₃S₂ to form Ni₃S₂/carbon composites is also a feasible method. In the Ni₃S₂/carbon composites, carbon not only stabilizes the interface between the electrode and the electrolyte, but also improves the overall conductivity.^{32,33} Among the Ni₃S₂/carbon composites, carbon-coated Ni₃S₂ nanoparticles with full protection present excellent performance; however, the point-to-point contact among carbon-coated Ni₃S₂ particles may hinder the rapid transfer of electrons from the carbon to the active material, which cannot support a fast charge and discharge process.^{34–36} Hence, it is still a great challenge to rationally composite carbon and Ni₃S₂ to obtain optimum high-rate Ni₃S₂ anodes for SIBs.

Herein, we designed a unique Ni₃S₂/carbon hierarchical microstructure by anchoring graphitic-carbon-coated Ni₃S₂ particles on N-doped mesoporous carbon nanoflakes. The N-doped mesoporous carbon nanoflakes, together with the graphitic carbon, would work as a platform to provide fast electron transport and Na⁺ diffusion, and the graphitic carbon layer can also relieve the strain caused by the volume expansion. As a result, the final Ni₃S₂/carbon composite can achieve an ultrahigh rate cycling performance when applied as an anode for SIBs.

Experimental

Chemicals

NiCl₂·6H₂O (≥99.0%), CH₃COONa (≥99.0%) and ethylene glycol (EG) were purchased from Sinopharm Chemical Reagent Co., Ltd. Dopamine hydrochloride (≥98.0%), tris (hydroxymethyl) aminomethane hydrochloride (≥99.0%) and thioacetamide were supplied by Sigma-Aldrich Co. LLC. All chemicals were used directly as received without further purification.

Sample preparation

Synthesis of the nickel-based precursor

The nickel-based precursor was synthesized according to our previous work.¹⁶ In a typical synthesis, 0.01 mol of $\text{NiCl}_2 \cdot 6\text{H}_2\text{O}$ and 0.09 mol of CH_3COONa were dissolved in a total volume of 80 ml EG. Then, the mixture was transferred and sealed in a 100 ml Teflon-lined stainless-steel autoclave and maintained at 200 °C for 8 h to synthesize the nickel-based precursor.

Synthesis of the Ni@NC composites

600 mg of the above-synthesized nickel-based precursor was scattered in 300 ml of Tris-HCl buffer solution. Dopamine hydrochloride was then added, and the mixed solution was vigorously stirred at 30 °C for 12 h. A black solid was obtained after washing with deionized water and ethanol. Three samples, denoted as Ni@PDA-1, Ni@PDA-2, and Ni@PDA-3, were obtained by adjusting the amount of dopamine to 225 mg, 375 mg, and 600 mg, respectively. Finally, the three Ni@PDA samples were pyrolyzed at 800 °C for 4 h under an argon atmosphere to prepare Ni@NC-1, Ni@NC-2, and Ni@NC-3.

Synthesis of the Ni_3S_2 @NC composites

200 mg of as-prepared Ni@NC and 250 mg of thioacetamide were co-dissolved in 80 ml of deionized water and reacted at 160 °C for 4 h. The black solid–liquid mixture in the autoclave was then washed with deionized water several times to obtain the final Ni_3S_2 @NC composite. Similarly, three other sulfurized samples were prepared, Ni_3S_2 @NC-1, Ni_3S_2 @NC-2 and Ni_3S_2 @NC-3.

Materials characterization

X-ray diffraction (XRD) measurements were performed using an ultima IV instrument with $\text{Cu K}\alpha$ radiation. Fourier transform infrared spectroscopy (FTIR) was carried out using a Nicolet IS5 instrument. Raman spectra were collected using a HR800 instrument. A nitrogen adsorption analyzer (ASAP2020) was used to characterize the pore structure. Scanning electron microscopy (SEM, Hitachi SU8010) and transmission electron microscopy (TEM, JEM-ARM200F) were used to observe the microstructure and morphology. Thermogravimetric analysis (TGA) (Netzsch STA 449 F3) was performed under an air atmosphere to analyze the carbon content in the composites. X-ray photoelectron spectroscopy (XPS) measurements were carried out using a Thermo Scientific ESCALAB 250Xi spectrometer.

Electrochemical characterization

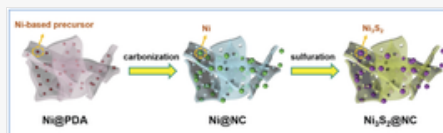
The electrochemical tests were performed using a CR2032-type coin cell assembly with sodium as the counter electrode in an argon-filled glovebox. The working electrode was fabricated by coating a slurry (Ni_3S_2 @NC, ketjen black, and polyvinylidene fluoride in a mass ratio of 8 : 1 : 1) on copper foil. After being completely dried, the electrode was perforated into a circle with a diameter of 12 mm, in which the active material load weight was *ca.* 1.0 mg cm^{-2} . The electrolyte was 1.0 M NaCF_3SO_3 in diglyme, and the separator was glass fiber (GF/F). The cycle and rate performances were measured using Land CT2001A battery test systems. Cyclic voltammetry (CV) curves were measured on a CHI-660E electrochemical workstation.

Results and discussion

In this study, the Ni_3S_2 /carbon composite was obtained by replicating the nanoflake-assembled nickel-based precursor, and the detailed construction process is illustrated in Scheme 1. First, the nickel-based precursor was synthesized according to our previous study,¹⁶ and a scanning electron microscopy (SEM) image shows a nanoflake-assembled microstructure whose flake thickness was measured to be *ca.* 11 nm (Fig. S1[†]). Subsequently, a layer of polydopamine (PDA) was coated on the surface of the nanoflakes of the nickel-based precursor, and the obtained samples, denoted as Ni@PDA, retained the nanoflake-assembled morphology of the nickel-based precursor (Fig. 1a–c). When the amount of dopamine added in the reaction system was adjusted, the thicknesses of the resulting nanoflakes were measured to be *ca.* 12 nm, 23 nm, and 51 nm for samples Ni@PDA-1, Ni@PDA-2, and Ni@PDA-3, respectively. The Ni@PDA composite was then carbonized at a high temperature of 800 °C to convert the PDA into N-doped carbon, and the

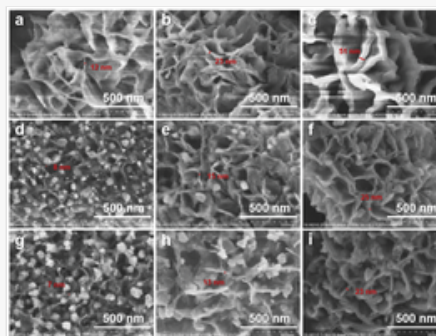
corresponding Ni/N-doped carbon samples (denoted as Ni@NC) were obtained. In the three Ni@NC samples, the Ni species were all confirmed to be zero-valent nickel (Fig. S2[†]). The SEM images in Fig. 1d–f show that the nanoflake-assembled skeletons still existed in the three Ni@NC samples, and based on measurement from the SEM images, the thicknesses of the nanoflakes were *ca.* 8 nm, 15 nm, and 25 nm, respectively, which are much thinner than those of the corresponding Ni@PDA samples. However, unlike in Ni@PDA, there are some Ni particles scattered on the surface of the nanoflakes, and the amount of particles is negatively correlated with the thickness of the nanoflake, demonstrating that more Ni particles can be confined by thicker carbon flakes. After solution vulcanization, the final nickel sulfide/N-doped carbon (Ni₃S₂@NC) almost completely maintained the morphology of the corresponding Ni@NC sample, with slightly thinned nanoflakes and enlarged nickel sulfide particles (Fig. 1g–i).

Scheme 1



Schematic diagram of the synthesis route of the Ni₃S₂/carbon composite.

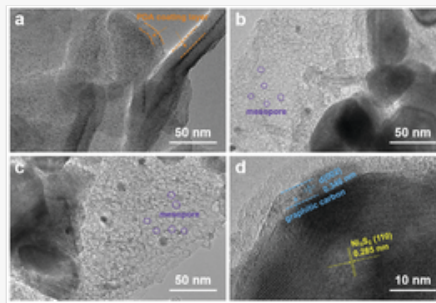
Fig. 1



SEM images of (a–c) Ni@PDA-1, -2 and -3, (d–f) Ni@NC-1, -2 and -3, and (g–i) Ni₃S₂@NC-1, -2 and -3.

TEM measurement was then performed on Ni@PDA-3, Ni@NC-3 and Ni₃S₂@NC-3 to investigate the structure evolution during the synthetic process, as Ni@PDA-3 had the thickest nanoflakes, which would make it easier to observe the process of structure evolution. As seen in the TEM image of Ni@PDA-3 (Fig. 2a), the nanoflake displays a sandwiched structure in which the nickel-based precursor constructed with 3 nm nanoparticles is encapsulated by PDA. After carbonization, the carbon nanoflake of sample Ni@NC-3 (Fig. 2b) exhibits many mesopores with a pore size of *ca.* 6.5 nm and some nickel particles inlaid in the plane of the carbon flake. As is known, in the nickel-based precursor, the 3 nm nanoparticles possessed high surface energy and had a tendency towards agglomeration; hence, during the high-temperature carbonization, the nickel-based precursor was reduced and grew into large zero-valent nickel particles, and some mesopores were left in the corresponding carbon nanoflake. Fig. 2c shows the nanostructure of Ni₃S₂@NC-3, which displays almost the same morphology as Ni@NC-3, and is composed of mesoporous carbon and larger-sized particles. By increasing the resolution of the TEM measurement (Fig. 2d), graphitic carbon formed through a catalytic process of Ni during carbonization is found to be coated on the surface of the Ni₃S₂ particles. The graphitic carbon thickness was measured to be *ca.* 3.2 nm, and the corresponding interlayer distance (d_{002}) was measured to be *ca.* 0.346 nm, which is beneficial for conductivity and Na⁺ insertion. Furthermore, the interplanar spacing of the Ni₃S₂ nanocrystal was calculated to be *ca.* 0.285 nm, corresponding to its (110) crystal plane. Similarly, Ni₃S₂@NC-1 and Ni₃S₂@NC-2 also have analogous morphologies (Fig. S3[†]) with coexisting mesoporous carbon flakes and graphitic-carbon-coated Ni₃S₂ nanoparticles.

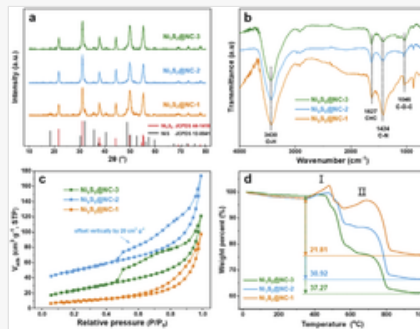
Fig. 2



TEM images of (a) Ni@PDA-3, (b) Ni@NC-3, and (c and d) Ni₃S₂@NC-3.

The chemical compositions and structures of the as-prepared Ni₃S₂@NC composites were characterized using XRD, FTIR, and Raman spectroscopy and N₂ sorption measurements. As seen in the XRD patterns in Fig. 3a, the nickel species of the three samples consist mainly of Ni₃S₂ (JCPDS: 44-1418) with less than 2% NiS (JCPDS: 12-0041). The FTIR spectra (Fig. 3b) of the three Ni₃S₂@NC composites display strong peaks characteristic of C–N stretching vibrations at 1424 cm⁻¹, indicating the formation of N-doped carbon. The two characteristic peaks in the Raman spectra (Fig. S4[†]) located at around 1329 cm⁻¹ and 1574 cm⁻¹ stem from the typical D- and G-bands of carbon, respectively.

Fig. 3



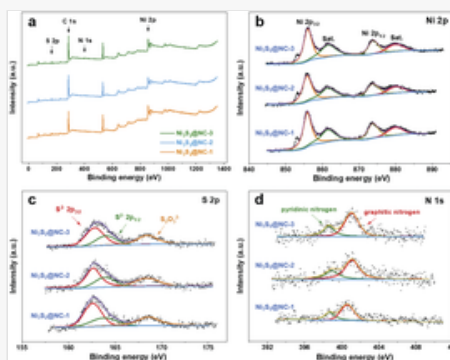
(a) XRD patterns, (b) FTIR spectra, (c) N₂ sorption isotherms and (d) TGA curves of the Ni₃S₂@NC-1, Ni₃S₂@NC-2 and Ni₃S₂@NC-3.

The N₂ sorption isotherms of the three Ni₃S₂@NC composites with type IV hysteresis are shown in Fig. 3c, revealing the characteristics of their mesoporous structures. The pore size distribution of the sample Ni₃S₂@NC-3 is centred at *ca.* 6.25 nm (Fig. S5[†]), which is highly consistent with the TEM measurements. Thermogravimetric analysis (TGA) was then performed on the three samples to quantitatively analyse their carbon content. As shown in Fig. 3d, there are four main weight-change stages with increasing temperature from 30 °C to 1000 °C under an air atmosphere. The slight weight loss below 350 °C can be attributed to the removal of adsorbed water. Subsequently, the first weight-increase stage (I) at *ca.* 450 °C is due to the conversion of Ni₃S₂ to NiS and a small amount of NiO (Fig. S6a[†]). As the oxidation progresses, all the NiS is oxidized to NiSO₄ (Fig. S6b[†]), causing a second (II) weight-increase stage. When the reaction proceeds to 800 °C, all the products are oxidized to NiO (Fig. S6c[†]), which is stable at around 1000 °C. That is, the weight change from 350 °C to 1000 °C corresponds to the consumption of the carbon components and the conversion of Ni₃S₂ to NiO. Hence, based on the retained mass at 1000 °C, the carbon contents in Ni₃S₂@NC-1, Ni₃S₂@NC-2 and Ni₃S₂@NC-3 were calculated to be *ca.* 16.2%, 26.0% and 32.8%, respectively (the detailed calculation process is shown in the ESI[†]).

XPS measurements were conducted to evaluate the chemical identities and valence states of the Ni₃S₂@NC nanocomposites. As seen in Fig. 4a, the survey spectra demonstrate the coexistence of the elements S (163 eV), C (284 eV), N (401 eV), and Ni (856 eV) in all three samples. In the high-resolution spectrum of Ni 2p in Fig. 4b, the two distinct peaks located at 873.7 eV and 856.1 eV accompanied by the corresponding satellite peaks at 861.7 and 880.2 eV can be assigned to Ni 2p_{1/2} and Ni 2p_{3/2}, respectively. In the S 2p region (Fig. 4c), the peaks at 164.0 eV and 162.8

eV are derived from S 2p_{1/2} and S 2p_{3/2} of S²⁻, while the peak at around 168.5 eV is expected to arise from the residual S₂O₃²⁻ on the surface of Ni₃S₂@NC. In the C 1s region (Fig. S7[†]), the peaks observed at around 284.4, 285.1, 286.2 and 288.5 eV can be attributed to C-C/C=C, C-N, C-O and O=C-O, respectively. There are no C-S related species in the final Ni₃S₂@NC composites, demonstrating that low-temperature vulcanization cannot achieve vulcanization on the carbon skeleton. Moreover, two forms of N species, pyridinic N (398.6 eV) and graphitic N (401.0 eV), can be visually observed in the N 1s spectrum (Fig. 4d). Pyridinic N is known to be able to enhance the surface-induced capacitive processes and increase the diffusion kinetics of the sodium ion, while graphitic N is believed to modify the electrical conductivity of the carbon framework due to the change in the electron-donor characteristics; thereby, the N-containing groups would improve the electrochemical performance of the resultant material.

Fig. 4

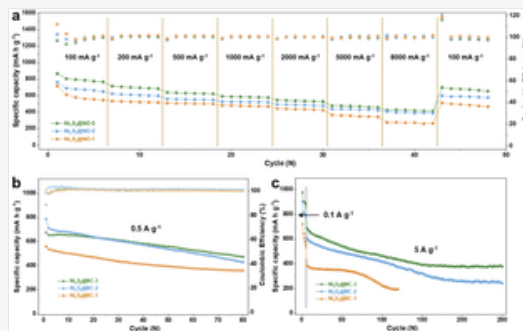


(a) XPS survey spectra and the corresponding deconvoluted peaks of (b) Ni 2p, (c) S 2p and (d) N 1s in the high resolution XPS spectra of the Ni₃S₂@NC-1, Ni₃S₂@NC-2 and Ni₃S₂@NC-3.

Electrochemical tests of the three Ni₃S₂@NC composites were then carried out, and the capacities were calculated based on the composites. The rate capabilities of the three samples are shown in Fig. 5a; Ni₃S₂@NC-3 delivers the highest average charge capacities of 800, 700, 631, 585, 537, 469, and 421 mA h g⁻¹ as the current density is increased from 100 to 8000 mA g⁻¹, respectively. Furthermore, when the current density is reset to 100 mA g⁻¹, it recovers to ca. 677 mA h g⁻¹. However, the Ni₃S₂@NC-2 and Ni₃S₂@NC-1 electrodes deliver reversible capacities of only 687, 610, 554, 524, 486, 431, and 396 mA h g⁻¹ and 596, 525, 505, 476, 435, 354, and 270 mA h g⁻¹ at corresponding current densities. The initial coulombic efficiencies (ICE) of Ni₃S₂@NC-1 and Ni₃S₂@NC-2 are 112.0% and 102.7%, respectively, where a CE higher than 100% implies loss of the active materials. As sodium sulfides are considered to be the most common discharge products of the conversion reaction between metal sulfides and sodium, polysulfides are a possible intermediate, and are soluble in the ether-based electrolyte.³⁷ If the Ni₃S₂ particles are not well protected by the carbon matrix, during the discharge process, the *in situ* formed polysulfide intermediate can be dissolved into the electrolyte, leading to active material loss. During the subsequent charge process, overcharge occurs as the dissolved polysulfides can cause a large voltage polarization, giving an ICE higher than 100%. Satisfactorily, the ICE of Ni₃S₂@NC-3 is 97.0%, demonstrating effective protection of Ni₃S₂ by the graphitic carbon and N-doped carbon. The cyclic voltammetry (CV) curves and galvanostatic discharge-charge voltage profiles (Fig. S8[†]) demonstrate the reduction of Ni₃S₂ to Ni and the oxidation of Ni to Ni₃S₂ in the discharge and charge processes, respectively.

Fig. 5

Figure Replacement Requested



(a) Rate capability at different current densities, and cycling performances at (b) 0.5 A g⁻¹ and (c) 5 A g⁻¹ of Ni₃S₂@NC-1, Ni₃S₂@NC-2 and Ni₃S₂@NC-3.

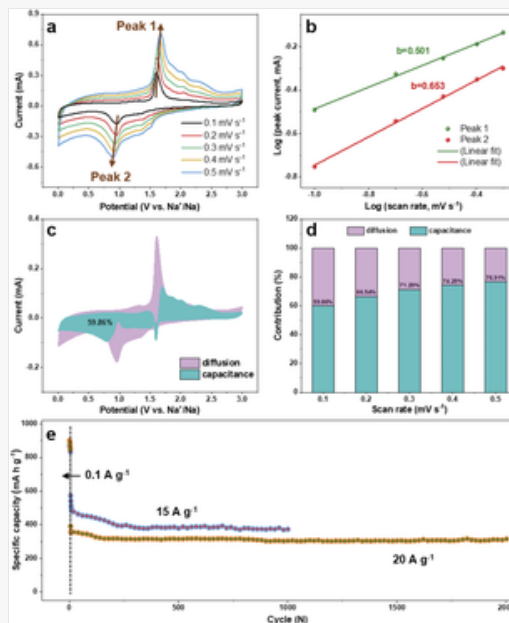
Replacement Image: Fig.5.tif

Replacement Instruction: Replace image requested

Fig. 5b compares the cycling performance of the three Ni₃S₂@NC composites at a current density of 0.5 A g⁻¹. Among the three samples, Ni₃S₂@NC-2 shows the highest initial charge capacity of *ca.* 787 mA h g⁻¹; however, after 80 cycles, Ni₃S₂@NC-3 delivers a reversible capacity of 473 mA h g⁻¹, which is higher than that of Ni₃S₂@NC-2 (429 mA h g⁻¹) and Ni₃S₂@NC-1 (359 mA h g⁻¹). Remarkably, Ni₃S₂@NC-1 still displays an ICE of 101.1%, higher than 100%, and in the following 10 cycles, the CE presents a slight decrease and remains stable at around 100%. The three samples were further cycled with the current density being changed from 0.1 to 5 A g⁻¹ after five galvanostatic charge–discharge cycles (Fig. 5c). The initial charge capacities were 976, 904 and 720 mA h g⁻¹, respectively, for Ni₃S₂@NC-3, Ni₃S₂@NC-2 and Ni₃S₂@NC-1. In the following cycles, the capacity of Ni₃S₂@NC-2 is only *ca.* 243 mA h g⁻¹ after another 245 cycles, and Ni₃S₂@NC-1 suffers from a severe capacity loss, maintaining only 194 mA h g⁻¹ after 120 cycles. Ni₃S₂@NC-3 exhibits a gradual capacity decay and then remains stable at around 376 mA h g⁻¹ until 250 cycles. This cycling stability may be attributed to its hierarchical microstructure constructed with well-embedded graphitic-carbon-coated Ni₃S₂ in N-doped mesoporous carbon nanoflakes, which is expected to provide high accessibility to the electrolyte, retard self-aggregation, avoid active material loss, buffer volume expansion, and provide fast Na⁺ diffusion and electron transport during charge–discharge processes, finally achieving high capacity and excellent cycling stability.

To further explain the sodium storage mechanism of Ni₃S₂@NC-3, CV tests at different scan rates were performed to investigate its redox pseudo-capacitance contribution. The CV curves at different scan rates from 0.1 to 0.5 mV s⁻¹ (Fig. 6a) have similar shapes, and show minor polarization between Na⁺ insertion and extraction. Through linear fitting of the log(peak current) and log(scan rate) plot in Fig. 6b, the *b* values of the anode peak and cathode peak of Ni₃S₂@NC-3 were calculated to be 0.501 and 0.653, respectively, indicating that both the diffusion-controlled process and capacitance behavior of the Ni₃S₂@NC-3 composite have an impact on its electrochemical performance. At a scan rate of 0.1 mV s⁻¹, the contribution of the capacitive current to the total measured current was evaluated, as shown in Fig. 6c, of which 59.86% was quantified as the capacitance current. As the scan rate was increased from 0.1 to 0.5 mV s⁻¹ (Fig. 6d), the capacitive contribution ratios exhibited a progressive increase from 59.86% to 76.91%, while the diffusion behaviour of Ni₃S₂@NC-3 was suppressed. The desirable pseudocapacitive behaviour can be attributed to the N-doped mesoporous carbon, which provides convenient charge-transfer pathways for ultrafast Na-ion batteries. The impedance changes at the open circuit voltage and after the initial discharge were also investigated. In Fig. S9,[†] a depressed semicircle located at the high frequency area and an inclined line in the low-frequency area are presented in the Nyquist plots, with the electrode after discharge showing a lower charge transfer resistance (*R*_{ct}) than that of the pristine electrode, indicating excellent charge-transfer kinetics.

Fig. 6



Kinetic analysis of the sodium storage contributions for the $\text{Ni}_3\text{S}_2@\text{NC-3}$ electrode: (a) CV curves at scan rates from 0.1 to 0.5 mV s^{-1} ; (b) plots of the relationship between the $\log(\text{scan rate})$ and $\log(\text{peak current})$ for the cathodic and anodic CV sweeps; (c) fitted pseudo-capacitive contribution at 0.1 mV s^{-1} and (d) contribution ratio of the capacitance- and diffusion-controlled capacities at different scan rates. (e) Long-term cycling stability of $\text{Ni}_3\text{S}_2@\text{NC-3}$ at current densities of 15 A g^{-1} and 20 A g^{-1} .

Fig. 6e shows the ultrafast charge–discharge performance of the $\text{Ni}_3\text{S}_2@\text{NC-3}$. After five-cycle activation at a low current of 0.1 A g^{-1} , the $\text{Ni}_3\text{S}_2@\text{NC-3}$ electrode retains a high reversible charge capacity of 372 mA h g^{-1} at a current density of 15 A g^{-1} after another 995 cycles. Furthermore, when the current density is increased to 20 A g^{-1} , a capacity of 390 mA h g^{-1} is obtained and a reversible capacity of 316 mA h g^{-1} is maintained after 2000 cycles, which represents only 0.0375 mA h g^{-1} capacity loss per cycle. That is, the SIB can finish charging to 316 mA h g^{-1} within 1 min. However, in clear contrast, the other two samples cannot be cycled for 100 cycles, even at a current density of 8 A g^{-1} (Fig. S10[†]). To the best of our knowledge, $\text{Ni}_3\text{S}_2@\text{NC-3}$ exhibits the most excellent electrochemical performance among all the reported Ni_3S_2 -based electrodes for SIBs (see Table S1[†]).

Conclusions

In this study, $\text{Ni}_3\text{S}_2@\text{NC}$ composites were synthesized through a hydrothermal, high-temperature carbonization and vulcanization process and then successfully applied as electrode materials for SIBs. Among the composites, $\text{Ni}_3\text{S}_2@\text{NC-3}$ with a carbon content of 32.8% displayed a unique structure with well-embedded graphitic-carbon-coated Ni_3S_2 particles in the N-doped mesoporous carbon nanoflakes, which stabilized a charge capacity of 372 mA h g^{-1} at 5 A g^{-1} over 250 cycles, and even at 20 A g^{-1} , a reversible charge capacity of 316 mA h g^{-1} was maintained after 2000 cycles, indicating extremely excellent high-rate and long-cycle stability. This hierarchical structure combining mesoporous carbon nanoflakes and a graphitic carbon coating can provide a new strategy for the further development of electrode materials.

Author contributions

Jia-Lin Xu: Data curation, investigation, writing – original draft. Qiang Sun: Conceptualization, data curation, supervision, writing – review & editing. Hao-Jie Chen: Investigation. Wen-Jie Yan, formal analysis. Pai Lu: Data curation, supervision, writing – review & editing.

Conflicts of interest

There are no conflicts to declare.

Acknowledgements

This work is financially supported by the National Natural Science Foundation of China (No. 51902044, and 21503033) and the Fundamental Research Funds for the Central Universities (N2025021). The authors thank Yong-

 References can be edited in the panel that appears to the right when you click on a reference.

- 1 X. Zhao, F. Gong, Y. Zhao, B. Huang, D. Qian, H.-E. Wang, W. Zhang and Z. Yang, *Chem. Eng. J.*, 2020, **392**, 123675.
- 2 S. Fan, S. Huang, Y. Chen, Y. Shang, Y. Wang, D. Kong, M. E. Pam, L. Shi, Y. W. Lim, Y. Shi and H. Y. Yang, *Energy Storage Mater.*, 2019, **23**, 17–24.
- 3 C. Chen, M. Wu, J. Liu, Z. Xu, K. Zaghbi and Y. Wang, *J. Power Sources*, 2020, **471**, 228455.
- 4 X. Wu, S. Li, Y. Xu, B. Wang, J. Liu and M. Yu, *Chem. Eng. J.*, 2019, **356**, 245–254.
- 5 J. Chen, D. H. C. Chua and P. S. Lee, *Small Methods*, 2020, **4**, 1900648.
- 6 M. Leng, J. Bi, Z. Xing, W. Wang, X. Gao, J. Wang and Z. Zhao, *Chem. Eng. J.*, 2021, **413**, 127824.
- 7 H. Li, T. Wang, X. Wang, G. Li, Y. Du, J. Shen and J. Chai, *J. Power Sources*, 2021, **494**, 229771.
- 8 Y. Shi, Z. Zhang, P. Jiang, A. Gao, K. Li, Q. Zhang, Y. Sun, X. Lu, D. Cao and X. Lu, *Energy Storage Mater.*, 2021, **37**, 354–362.
- 9 Y. Liu, Y. Fang, Z. Zhao, C. Yuan and X. W. Lou, *Adv. Energy Mater.*, 2019, **9**, 1803052.
- 10 Z. Chen, R. Wu, M. Liu, H. Wang, H. Xu, Y. Guo, Y. Song, F. Fang, X. Yu and D. Sun, *Adv. Funct. Mater.*, 2017, **27**, 1702046.
- 11 W. Liu, X. Yuan and X. Yu, *Nanoscale*, 2018, **10**, 16675.
- 12 H. Han, X. Chen, J. Qian, F. Zhong, X. Feng, W. Chen, X. Ai, H. Yang and Y. Cao, *Nanoscale*, 2019, **11**, 21999.
- 13 H. Huang, R. Xu, Y. Feng, S. Zeng, Y. Jiang, H. Wang, W. Luo and Y. Yu, *Adv. Mater.*, 2020, **32**, 1904320.
- 14 L. Shen, Y. Wang, F. Wu, I. Moudrakovski, P. A. Aken, J. Maier and Y. Yu, *Angew. Chem., Int. Ed.*, 2019, **58**, 7238–7243.
- 15 T. A. Ho, C. Bae, H. Nam, E. Kim, S. Y. Lee, J. H. Park and H. Shin, *ACS Appl. Mater. Interfaces*, 2018, **10**, 12807–12815.
- 16 J.-L. Xu, L. Liu, Y.-H. Sun, W.-J. Yan, Z.-R. Wang and Q. Sun, *J. Alloys Compd.*, 2020, **835**, 155418.
- 17 X. Xia, Q. Wang, Q. Zhu, J. Xie, J. Wang, D. Zhuang, S. Zhang, G. Cao and X. Zhao, *Mater. Today Energy*, 2017, **5**, 99–106.

- 18 Z. Zhao, Z. Hu, R. Jiao, Z. Tang, P. Dong, Y. Li, S. Li and H. Li, *Energy Storage Mater.*, 2019, **22**, 228–234.
- 19 H. Li, H. Yang, Z. Sun, Y. Shi, H.-M. Cheng and F. Li, *Nano Energy*, 2019, **56**, 100–108.
- 20 Y. Zhang, P. Wang, Y. Yin, X. Zhang, L. Fan, N. Zhang and K. Sun, *Chem. Eng. J.*, 2019, **356**, 1042–1051.
- 21 M. Mao, C. Cui, M. Wu, M. Zhang, T. Gao, X. Fan, J. Chen, T. Wang, J. Ma and C. Wang, *Nano Energy*, 2018, **45**, 346–352.
- 22 L. Chen, M. Shen, S.-B. Ren, Y.-X. Chen, W. Li and D.-M. Han, *Nanoscale*, 2021, **13**, 9328–9338.
- 23 Y. Li, J. Qian, M. Zhang, S. Wang, Z. Wang, M. Li, Y. Bai, Q. An, H. Xu, F. Wu, L. Mai and C. Wu, *Adv. Mater.*, 2020, **32**, 2005802.
- 24 Y. Wang, Y. Zhang, Y. Peng, H. Li, J. Li, B.-J. Hwang and J. Zhao, *Electrochim. Acta*, 2019, **299**, 489–499.
- 25 W. Shuang, H. Huang, L. Kong, M. Zhong, A. Li, D. Wang, Y. Xu and X.-H. Bu, *Nano Energy*, 2019, **62**, 154–163.
- 26 J. Li, J. Li, Z. Ding, X. Zhang, Y. Li, T. Lu, Y. Yao, W. Mai and L. Pan, *Chem. Eng. J.*, 2019, **378**, 122108.
- 27 J. Tang, S. Ni, D. Chao, J. Liu, X. Yang and J. Zhao, *Electrochim. Acta*, 2018, **265**, 709–716.
- 28 Y. Han, S. Liu, L. Cui, L. Xu, J. Xie, X.-K. Xia, W.-K. Hao, B. Wang, H. Li and J. Gao, *Int. J. Miner. Metall. Mater.*, 2018, **25**, 88–93.
- 29 S. Zhou, A. Hu, D. Liu, X. Chen, Q. Tang, T. Tao and H. Chen, *Electrochim. Acta*, 2020, **339**, 135938.
- 30 M. Yang, Q. Ning, C. Fan and X. Wu, *Chin. Chem. Lett.*, 2021, **32**, 895–899.
- 31 H.-J. Chen, Y. Wang, X.-D. Ma, C. Fan, P. K. Shen, S.-W. Ta, H.-B. Wu and Z.-S. Feng, *J. Mater. Sci.*, 2020, **55**, 17081–17093.
- 32 J. Jiang, Z. Li, G. Nie, P. Nie, Z. Pan, Z. Kou, Q. Chen, Q. Zhu, H. Dou, X. Zhang and J. Wang, *Batteries Supercaps*, 2020, **3**, 1360–1369.
- 33 Y. Zhang, J. Meng, X. Wang, X. Liu, X. Xu, Z. Liu, K. A. Owusu, C. Huang, Q. Li and L. Mai, *Chem. Commun.*, 2018, **54**, 1469.
- 34 Y.-C. Xiao, C.-Y. Xu, P.-P. Wang, H.-T. Fang, X.-Y. Sun, F.-X. Ma, Y. Pei and L. Zhen, *Nano Energy*, 2018, **50**, 675–684.
- 35 Q. Hu, Y. Meng, H. Zhang, G. Zhao, J. Hu, F. Zhu and Y. Zhang, *J. Electroanal. Chem.*, 2020, **837**, 114383.
- 36 S. Wang, Y. Fang, X. Wang and X. W. Lou, *Angew. Chem., Int. Ed.*, 2019, **58**, 760–763.
- 37 Z. Hu, Q. Liu, S.-L. Chou and S.-X. Dou, *Adv. Mater.*, 2017, **29**, 1700606.

Footnotes

[†] Electronic supplementary information (ESI) available. See DOI: [10.1039/d1nr05539a](https://doi.org/10.1039/d1nr05539a)

Queries and Answers

Q1

Query: Funder details have been incorporated in the funder table using information provided in the article text. Please check that the funder information in the table is correct.

Answer: Yes, the information is correct.

Q2

Query: For your information: You can cite this article before you receive notification of the page numbers by using the following format: (authors), Nanoscale, (year), DOI: 10.1039/d1nr05539a.

Answer: ok

Q3

Query: Please confirm that the spelling and format of all author names is correct. Names will be indexed and cited as shown on the proof, so these must be correct. No late corrections can be made.

Answer: Yes, the spelling and format of all author names is correct.

Q4

Query: Please check that the inserted Graphical Abstract text is suitable. If you provide replacement text, please ensure that it is no longer than 250 characters (including spaces).

Answer: The inserted text is ok. But there is something wrong with the previous Graphical image, we have replaced it. Thanks.

Q5

Query: AU: In the Fig. 5 graphic, “Efficiency” is spelled incorrectly as “Effciency”. Please supply a corrected version of the image with your proof corrections, preferably as a TIF file at a resolution of at least 600 dpi.

Answer: Thanks, we have provided a corrected image.

Q6

Query: AU: In the sentence beginning “This cycling stability ...”, “discharge-discharge” has been changed to “charge–discharge”. Please check that the revised text reflects your intended meaning.

Answer: That is ok.